Journal of Molecular Modeling (2024) 30:268
https://doi.org/10.1007/s00894-024-06059-z

ORIGINAL PAPER

Quantum phase transitions in one-dimensional nanostructures: a comparison between DFT and DMRG methodologies

T. Pauletti[1] · M. Sanino[1] · L. Gimenes[1] · I. M. Carvalho[1] · V. V. França[1]

Received: 15 February 2024 / Accepted: 1 July 2024 / Published online: 16 July 2024

Abstract

Context In the realm of quantum chemistry, the accurate prediction of electronic structure and properties of nanostructures remains a formidable challenge. Density functional theory (DFT) and density matrix renormalization group (DMRG) have emerged as two powerful computational methods for addressing electronic correlation effects in diverse molecular systems. We compare ground-state energies ($\boldsymbol{e_0}$), density profiles ($\boldsymbol{n}$), and average entanglement entropies ($\bar{\boldsymbol{S}}$) in metals, insulators and at the transition from metal to insulator, in homogeneous, superlattices, and harmonically confined chains described by the fermionic one-dimensional Hubbard model. While for the homogeneous systems, there is a clear hierarchy between the deviations, $\boldsymbol{D\%(\bar{S}) < D\%(e_0) < \bar{D}\%(n)}$, and all the deviations decrease with the chain size; for superlattices and harmonic confinement, the relation among the deviations is less trivial and strongly dependent on the superlattice structure and the confinement strength considered. For the superlattices, in general, increasing the number of impurities in the unit cell represents lower precision in the DFT calculations. For the confined chains, DFT performs better for metallic phases, while the highest deviations appear for the Mott and band-insulator phases. This work provides a comprehensive comparative analysis of these methodologies, shedding light on their respective strengths, limitations, and applications.

Methods The DFT calculations were performed using the standard Kohn-Sham scheme within the BALDA approach. It integrated the numerical Bethe-Ansatz (BA) solution of the Hubbard model as the homogeneous density functional within a local-density approximation (LDA) for the exchange-correlation energy. The DMRG algorithms were implemented using the ITensor library, which is based on the matrix product states (MPS) ansatz. The calculations were performed until the energy reaches convergence of at least $\mathbf{10^{-8}}$.

Keywords Density functional theory · Density matrix renormalization group · Hubbard model · Quantum phase transitions · Entanglement

✉ I. M. Carvalho
isaac.carvalho@unesp.br

✉ V. V. França
vivian.franca@unesp.br

T. Pauletti
tatiana.pauletti@unesp.br

M. Sanino
marina.sanino@unesp.br

L. Gimenes
lucas.gimenes@unesp.br

[1] Institute of Chemistry, São Paulo State University, Francisco Degni 55, Araraquara 14800-090, São Paulo, Brazil

Introduction

Reliable predictions of nanostructure properties are essential for the development of advanced quantum technologies. Density functional theory (DFT) [1, 2] and density matrix renormalization group (DMRG) [3] methods stand out prominently in this pursuit. DMRG has demonstrated remarkable success in capturing strong correlation effects by systematically optimizing the wavefunction in a reduced Hilbert space, but gets computationally expensive with the size of the system.

On the other hand, DFT offers a cost-effective approach to study large systems and is widely used as an electronic

structure method. However, the inherent approximations in exchange-correlation functionals can lead to inaccuracies, particularly in strongly correlated systems. Despite of that Kohn-Sham DFT [4, 5] has been demonstrated to be reliable to describe for example *i)* transport properties in the weakly coupled repulsive regime [6], *ii)* phases in cold trapped atoms [7, 8], *iii)* charge gap [9], and *iv)* electrical response properties of homogeneous metals [10].

Within the context of strongly correlated systems modeled by the Fermi-Hubbard model [11, 12], previous studies have compared DMRG and DFT results across various scenarios [8, 10, 13–18]. For the quarter-filling case, small deviations (less than 2%) between the techniques for the ground-state energy and for the local densities have been reported [8, 10, 13]. However, finite size effects, confining potentials, increasing magnitude of onsite interactions, and band occupation approaching the half-filling case are generally associated with higher deviations [8, 14]. Nevertheless, a systematic comparison of DFT and DMRG in describing the electronic properties – and particularly entanglement measures – of quantum materials remains missing. Understanding the limitations and advantages of these methodologies is crucial for addressing quantum phase transitions in the Hubbard model, including the underlying mechanisms of exotic phases and high-temperature superconductors [19].

In this work, we provide a detailed comparative assessment of DFT and DMRG in nanostructures described by the one-dimensional Hubbard model. We explore homogeneous, superlattices, and harmonically confined chains, addressing key properties such as ground-state energies (e_0), density profiles (n), and average entanglement entropies ($\bar{S}$), the latter being commonly used to detect and characterize quantum phase transitions. While for the homogeneous systems, one finds a clear hierarchy between the deviations, $D\%(\bar{S}) < D\%(e_0) < \bar{D}\%(n)$, for superlattices and harmonically confined chains, the relation among deviations is non-trivial and dependent on the superlattice structure and the confinement strength adopted. For the superlattices, in general, increasing the number of impurities in the unit cell makes DFT calculations less precise. For the confined systems, DFT performs better for metallic phases, while the highest deviations appear for the Mott and band-insulator phases.

Model and methods

We consider one-dimensional (1D) systems described by the fermionic Hubbard Hamiltonian,

$$\hat{H} = -t\sum_{i,\sigma}(\hat{c}^{\dagger}_{i,\sigma}\hat{c}_{i+1,\sigma} + \hat{c}_{i,\sigma}\hat{c}^{\dagger}_{i+1,\sigma}) + U\sum_{i}\hat{n}_{i,\uparrow}\hat{n}_{i,\downarrow} + \sum_{i,\sigma}V_i\hat{n}_{i,\sigma}, \quad (1)$$

where $\hat{c}^{(\dagger)}_{i,\sigma}$ annihilates (creates) an electron with spin $\sigma = \uparrow, \downarrow$ at site i, and $\hat{n}_{i,\sigma} = \hat{c}^{\dagger}_{i,\sigma}\hat{c}_{i,\sigma}$ are number operators. The model considers nearest-neighbor hopping, on-site interactions, and local external potential terms with coefficients t, U, and V_i, respectively. The ground-state is calculated by fixing the total number of electrons N in a chain of size L and the total null magnetization, such that $\sum_i \langle \hat{n}_{i,\uparrow} \rangle = \sum_i \langle \hat{n}_{i,\downarrow} \rangle = N/2$. We consider different average densities $n = N/L$, restricted to $0 \leq n \leq 2$ (single energy band), and impose open boundary conditions at the chain ends. Throughout this work, we set $t = 1$, which defines the unit of energy.

At the limit $V_i = 0$, the Hamiltonian of Eq. 1 reduces to the standard Hubbard model. In this case, for $n < 1$, the ground-state represents a metallic phase, while for the half-filling ($n = 1$), the system consists of a Mott insulating phase for arbitrarily small $U > 0$ [20]. When V_i is periodically modulated, thus simulating superlattices (as in Fig. 1b), the potential may induce a quantum phase transition from metal to insulating [21–24]. Similarly, the Mott metal-insulator transition may be induced by the harmonic potential $V_i = k(i - L/2)^2$ (as in Fig. 1c) [25–28], widely used in state-of-the-art cold atoms experiments.

In this paper, we address the performance of DFT – when compared to numerically exact DMRG calculations – in describing the properties of the Hubbard model for all the

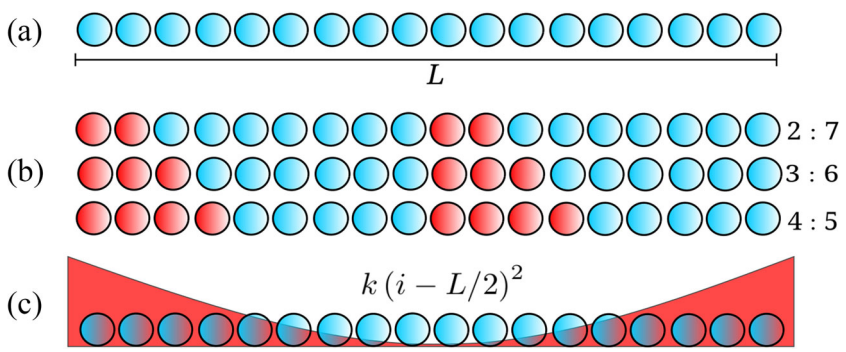

Fig. 1 Schematic setup of **a** a finite homogeneous lattice with $V_i = 0$ (blue circles), **b** superlattices with distinct modulations of the periodic $V_i \neq 0$ (red circles), for a fixed unit cell of 9 sites (2 : 7, 3 : 6, and 4 : 5), and **c** a chain under a harmonic confinement centered at $L/2$, $V_i = k(i - L/2)^2$

three 1D systems: homogeneous, superlattices, and harmonically confined chains, as schematically illustrated in Fig. 1.

We focus on three main quantities: the per-site ground-state energy e_0, the density profile $\{n_i\}$, and its respective nonlocal correlations, quantified by the average single-site entanglement

$$\bar{S} = \frac{1}{L}\sum_{i}^{L} S_i, \tag{2}$$

with

$$S_i = -\mathrm{Tr}[\rho_i \log_2 \rho_i] = -\sum_k \mathrm{w}_{i,k}\log_2 \mathrm{w}_{i,k}, \tag{3}$$

where $\mathrm{w}_{i,k}$ are the eigenvalues of the i-site reduced density matrix $\rho_i = \mathrm{Tr}_{L-1}[\rho_{GS}]$ calculated by tracing out the remaining $L-1$ sites from the ground-state density matrix ρ_{GS}. This type of entanglement has been proved to be relevant in analyzing the localization and itinerancy of the indistinguishable particles [29–31]. In the site-occupation basis, the reduced Hilbert space has dimension $d = 4$, and thus $\mathrm{w}_{i,k}$ are the occupation probabilities with $k = \uparrow, \downarrow, 2, 0$, such that $\sum_k \mathrm{w}_{i,k} = 1$. The set $\{\mathrm{w}_{i,k}\}$ can be calculated by firstly computing the paired probability $\mathrm{w}_{i,2} = \langle \hat{n}_{i\uparrow}\hat{n}_{i\downarrow}\rangle = \partial e_0/\partial U$. From this term, one obtains the remaining probabilities: the unpaired, $\mathrm{w}_{i,\uparrow} = \mathrm{w}_{i,\downarrow} = \langle \hat{n}_i \rangle/2 - \mathrm{w}_{i,2}$, and the empty probability $\mathrm{w}_{i,0} = 1 - \mathrm{w}_{i,\uparrow} - \mathrm{w}_{i,\downarrow} - \mathrm{w}_{i,2}$.

The DMRG algorithms were implemented in our group using the ITensor library [32]. This library is based on the matrix product states (MPS) ansatz. The precision of the MPS representations was essentially controlled by configuring the bond dimension $\mathcal{D}$, whose maximum is setting to approximately 3000. The computational cost of DMRG scales as $O(L\mathcal{D}^2)$. Although the bond dimension grows exponentially with L, in 1D, the area law [33] predicts a limit to its growth for Hamiltonians with short-range interactions, allowing a more optimized process. The performance of DMRG calculations is significantly influenced by the initialization procedure. In our approach, we start with initial guesses and employ a warm-up algorithm. We begin with small bond dimensions, typically set to 20 for the first sweeps. Additionally, we apply pinning fields to the sites at the ends of the chain to improve convergence, sometimes requiring over 100 sweeps to fully converge the results: up to 800 sweeps were utilized to reach an energy convergence of at least 10^{-8}. This initialization strategy ensures that the system naturally converges to a physical state, enhancing both the convergence and accuracy of the results.

Via DFT, the per-site ground-state energy e_0 and the density profile $\{n_i\}$ are obtained via standard Kohn-Sham scheme [4, 5], implemented in our group within BALDA approach: in which the numerical Bethe-Ansatz (BA) solution of the Hubbard model is considered as the homogeneous density functional within a local-density approximation (LDA) for the exchange-correlation energy (for a review, see [34]).

Now for the entanglement, which requires the energy derivative with respect to U, $\mathrm{w}_2 = \partial e_0/\partial U$, to avoid errors related to the numerical derivative of the BALDA approach described above, we adopt instead the analytical derivative of the FVC parameterization for the energy [13], which (for non-magnetized systems) is given by

$$\mathrm{w}_2^{FVC}(n,U) = \frac{2n}{\beta(n,U)}\frac{\partial\beta(n,U)}{\partial U}\cos\left(\frac{\pi n}{\beta(n,U)}\right) - \frac{2}{\pi}\frac{\partial\beta(n,U)}{\partial U}\sin\left(\frac{\pi n}{\beta(n,U)}\right), \tag{4}$$

where $\beta(n,U) = \beta(U)^{\sqrt[3]{U}/8}$ and the function $\beta(U)$ is determined from

$$\frac{\beta(U)}{\pi}\sin\left(\frac{\pi}{\beta(U)}\right) = 2\int_0^\infty \mathrm{d}x \frac{J_0(x)\,J_1(x)}{x\left(1+e^{Ux/2}\right)}, \tag{5}$$

with J_0 and J_1 the zero and first order Bessel functions, respectively. This analytical parametrization becomes exact by construction for *i)* $U \to 0$ (for which $\beta = 2$), *ii)* $U \to \infty$ ($\beta = 1$), and *iii)* $n = 1$ and any U ($0 \leqslant \beta \leqslant 1$). For other (n,U) regimes, the FVC parametrization provides a reasonable approximation to the full Beth-Ansatz [35, 36] solution.

We thus adopt Eq. 4 as approximation to the homogeneous chain and hence perform a LDA to obtain the double occupancy for the inhomogeneous systems:

$$\mathrm{w}_{i,2} \approx \mathrm{w}_{i,2}^{LDA} = \mathrm{w}_2^{FVC}(n,U)|_{n\to n_i}, \tag{6}$$

by using the density profile $\{n_i\}$ obtained via BALDA.

The percentage deviations between DFT and DMRG calculations are then, for the energy,

$$D\%(e_0) = \left|\frac{e_0^{\mathrm{DMRG}} - e_0^{\mathrm{DFT}}}{e_0^{\mathrm{DMRG}}}\right| \times 100, \tag{7}$$

for the average single-site entanglement,

$$D\%(\bar{S}) = \left|\frac{\bar{S}^{\mathrm{DMRG}} - \bar{S}^{\mathrm{DFT}}}{\bar{S}^{\mathrm{DMRG}}}\right| \times 100, \tag{8}$$

while for the density profiles, we quantify a mean percentage deviation, defined as

$$\bar{D}\%(n) = \frac{1}{M}\sum_i^M \left|\frac{n_i^{\mathrm{DMRG}} - n_i^{\mathrm{DFT}}}{n_i^{\mathrm{DMRG}}}\right| \times 100, \tag{9}$$

where the average in the latter equation is performed only within the M sites with non-negligible occupation, $n_i \geq$

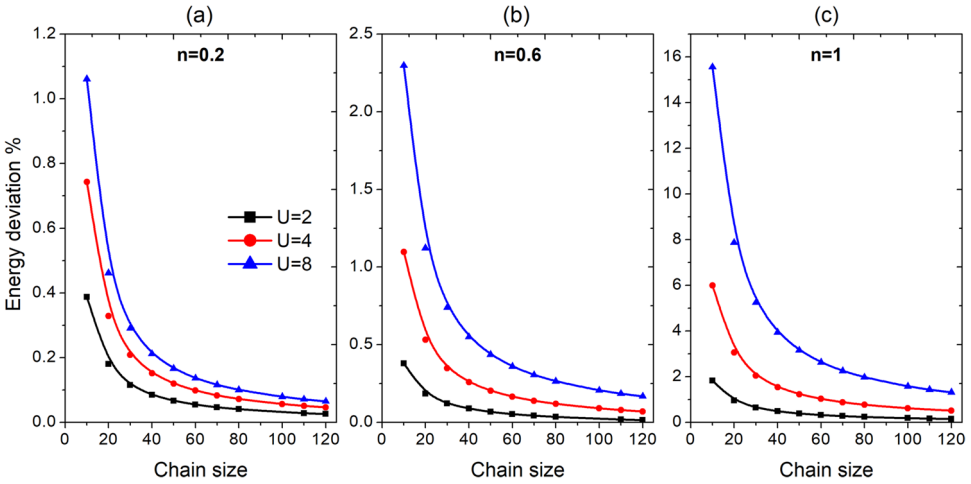

Fig. 2 DMRG-DFT deviation for the ground-state energy, Eq. 7, as a function of the chain length for a finite homogeneous system for low density **a**, intermediate density **b**, and at half-filling **c**, for several strengths of interaction U

0.001, in order to avoid artifactual amplification of the deviations.

Results and discussion

DFT x DMRG: homogeneous system

First, we analyze the DFT performance in reproducing the DMRG results for finite chains. In Fig. 2, we present the percentage deviation for the per-site ground-state energy. We see that in general, DFT performs better for low densities and weak interactions, in both cases, due to less influence of the electron–electron correlations. We find that the error monotonically decays by increasing the chain length L for all n, U, since our DFT-LDA approach becomes exact in the limit of $L \to \infty$.

Now, considering the DFT performance for the local densities $\{n_i\}$, we show in Fig. 3 the mean deviation defined in Eq. 9. For the Mott insulator regime, $n = 1$ and any $U > 0$, DFT is very precise with average deviations smaller than 0.004% due to the suppression of the Friedel-type oscillations [37, 38]. For the metallic regime, $n < 1$, the open ends of the chain act as effective impurities, inducing Friedel oscillations in the density distribution, which are not completely described by DFT, as can be confirmed by Fig. 4. Since the Friedel oscillations are more pronounced for low densities, the deviations are greater for $n = 0.2$ (Fig. 3a). In contrast, the smallest deviation for the energy is precisely for the case of $n = 0.2$ (Fig. 2a). We attribute this to error cancellations: while Eq. 9 sum up the local errors, the under and over DFT estimates for the density profile lead to error cancellation for the total energy. Nevertheless, for chain sizes $L \gtrsim 60$, DFT density profiles are also reliable, with mean deviations smaller than 2%.

For the average single-site entanglement, in Fig. 5, one finds a good performance of DFT calculations even for the worse regimes of parameters (for $L = 10$, $n = 1$, and $U = 4$): the maximum deviation observed is 1.73%. This very good performance of DFT for the average entanglement also

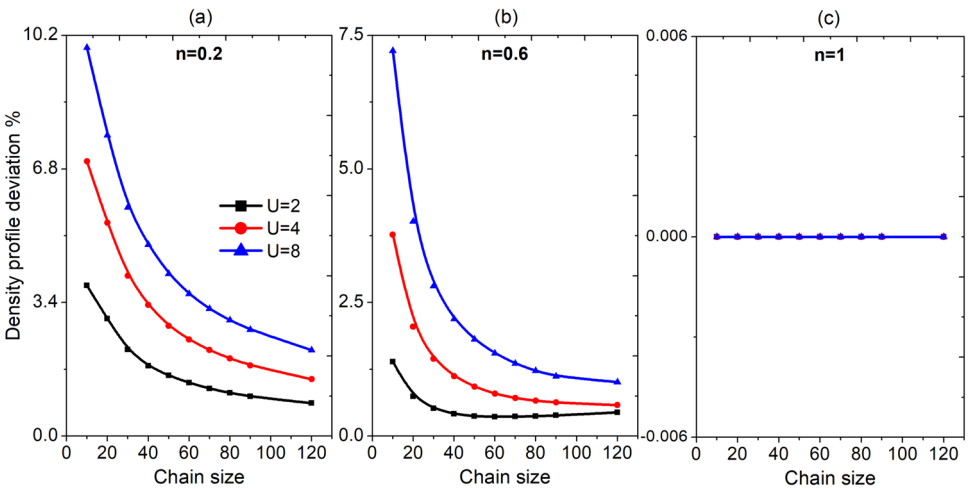

Fig. 3 Mean percentage deviation of the local densities, Eq. 9, as a function of the chain length for a homogeneous system at **a** $n = 0.2$, **b** $n = 0.6$, and **c** $n = 1$ for several values of U

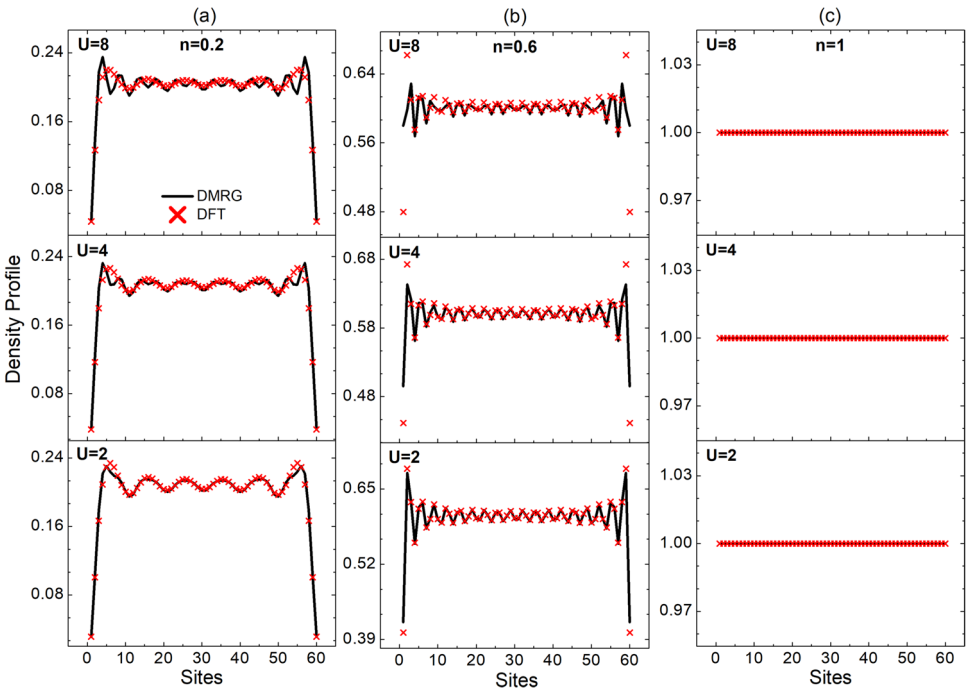

Fig. 4 Density profile for the homogeneous system with $L = 60$ sites, for several interactions U, and for distinct average filling factors: **a** $n = 0.2$, **b** $n = 0.6$, and **c** $n = 1$

comes from error cancellations: the von Neumann entropy is a density functional [29, 30]; thus, it reflects the DFT difficulty of reproducing the Friedel oscillations by under and overestimating the single-site entanglement along the chain, hence leading to a good average. As $\bar{S}$ has been widely used to detect and characterize quantum phase transitions [18, 31, 39–45], our results then show that DFT represents a reliable and powerful method to be used in Hubbard chains, as we explore below in inhomogeneous chains.

DFT x DMRG: superlattices

We focus on the performance of DFT calculations for identifying the Mott metal-insulator transition in superlattices

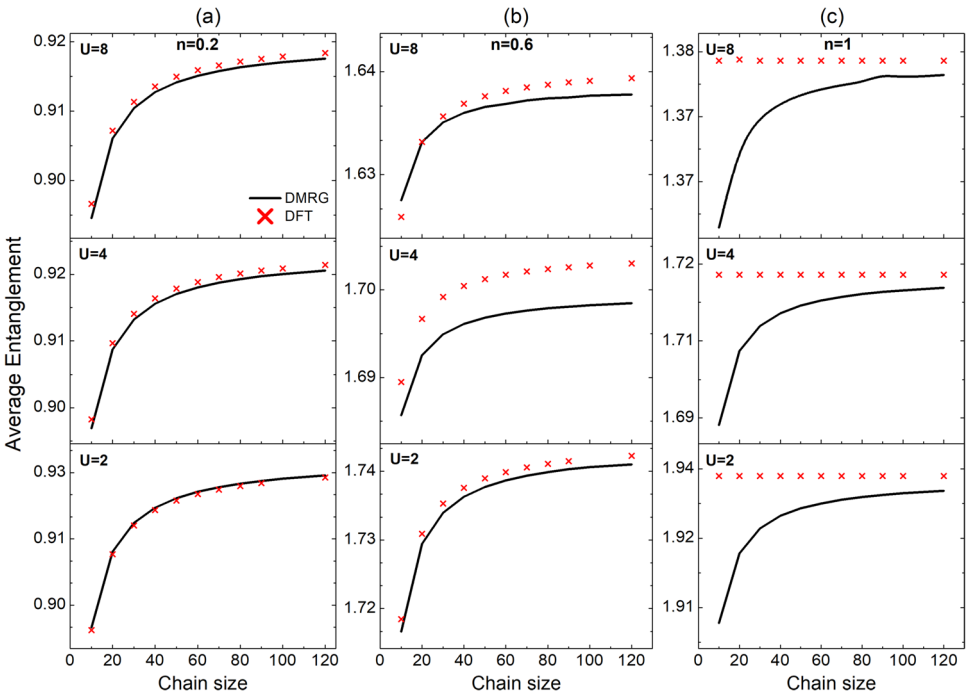

Fig. 5 Average entanglement $\bar{S}$ as a function of the chain length of homogeneous systems for several interaction regimes and different densities: $n = 0.2$ **a**, $n = 0.6$ **b**, and $n = 1$ **c**

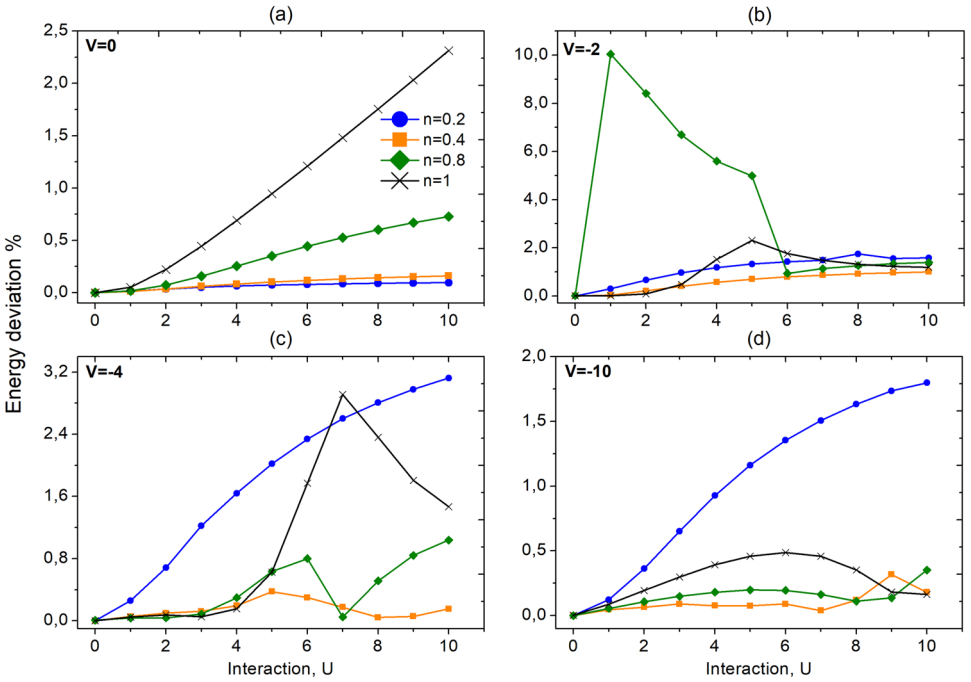

Fig. 6 DMRG-DFT deviation for the ground-state energy of the superlattice 2 : 7 with $L = 90$ sites as a function of interaction U, for several periodic potential strengths: **a** $V = 0$, **b** $V = -2$, **c** $V = -4$, and **d** $V = -10$

and harmonically confined chains. Starting with the superlattices (with unit cell SL 2 : 7), Fig. 6 shows that DFT is considerably precise in reproducing the ground-state energy: deviations increase in general by increasing the interaction U and the superlattice potential V, but are smaller than $\sim 3\%$ for all the regimes of parameters considered.

Accordingly, Fig. 7 reveals that also the density profile in the superlattice is reasonably well reproduced by DFT. For non-interacting systems, Fig. 7a, the density concentrates within the impurity sites, since the modulated potential is attractive, $V < 0$. For $U = 0$ and low average densities ($n = 0.2$ and $n = 0.4$), the particles essentially reside in the impurity sites, emptying the non-impurity ones. For higher

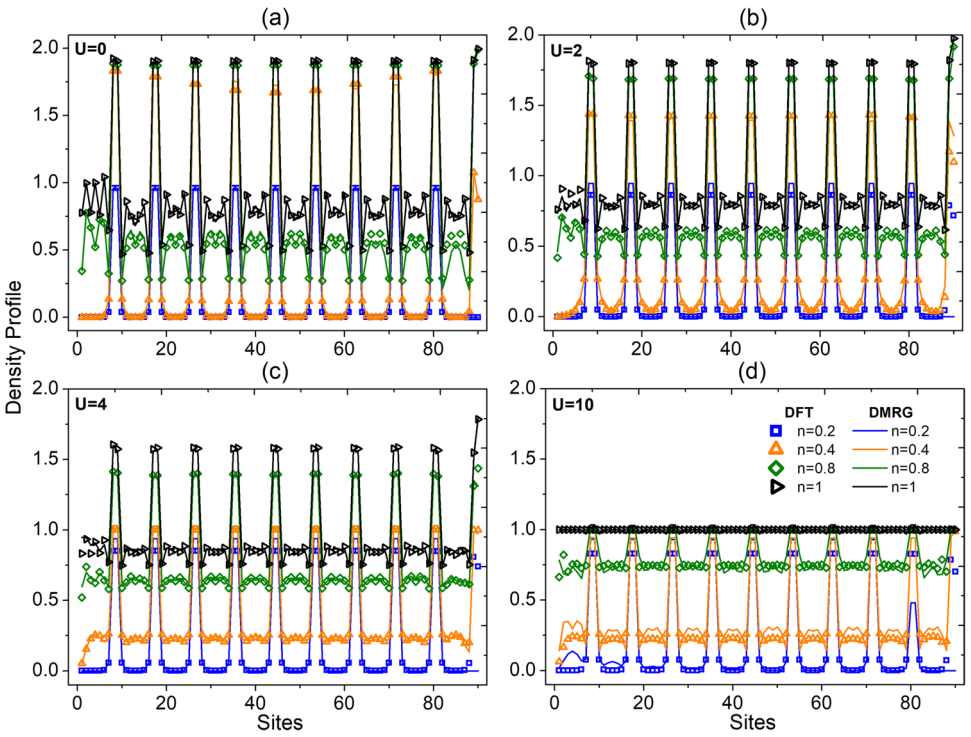

Fig. 7 Density profile for a superlattice 2 : 7 with $V = -4$, $L = 90$ sites, for several densities and distinct interactions: **a** $U = 0$, **b** $U = 2$, **c** $U = 4$, and **d** $U = 10$

average densities ($n = 0.8$ and $n = 1$), the impurity sites reach maximum occupation ($n_i = 2$); thus, the remaining particles are distributed also in the non-impurity sites.

When turning the interaction on, Fig. 7b–d, we find that the non-impurity sites start to be filled with particles even for the low density regime $n = 0.4$, once now the competition between $V < 0$ and $U > 0$ disfavors the maximum occupation at the impurity sites. Thus, depending on the three parameters V, n, U, the interaction can be strong enough to avoid $n_i > 1$ in the impurity sites, thus characterizing a local Mott insulator phase [21, 22]. This is seen already for $U \leq 2$ at $n = 0.2$, while at $n = 0.4$, this appears for $U \leq 4$ and at $n = 0.8$ and $n = 1$ only for $U \leq 10$, for this fixed $V = -4$.

We then analyze the average single-site entanglement as a function of U in order to find signatures of the Mott metal-insulator transition within the superlattice. As shown in Fig. 8, our results reveal that entanglement becomes non-monotonic with the density (crossing between distinct n curves) whenever the entire chain or a portion of it reaches the Mott-insulator regime: at $V = 0$ (homogeneous finite chain), it happens only for the $n = 1$ curve, once this is the only regime for the Mott physics in the absence of the superlattice potential. In contrast, depending on V, the non-monotonicity with n is observed also for $n < 1$, thus detecting the Mott insulator in a portion (the impurity sites) of the chain, as confirmed by Fig. 7. Consistently, we also see that the interaction for which the curves cross increases by increasing V, supporting the interpretation that the mechanism behind the Mott insulator phase in superlattices is the competition between U and V. Remarkably, DFT properly captures all this physics.

DFT x DMRG: harmonically confined systems

In Fig. 9, we present the DFT performance in recovering the DMRG ground-state energies for harmonically confined chains ($V_i = k(i - L/2)^2$) as a function of the potential curvature k. Although the deviations increase with the interaction, we find that for typical strongly correlated systems ($U = 4$), DFT energies deviate from DMRG by at most 2.5%, what can still be considered as a fair accuracy.

For the density profile, we find also a good agreement between the techniques, as can be seen in Fig. 10a. We also observe that the effective chain – defined by the central region where the particles are effectively distributed ($n_i > 0.001$) – decreases by increasing k, while the densities at the center of the chain increase. This occurs due to the strong potential at the wings. The density profile also reflects the metallic and insulating phases: (i) a metallic phase with $n_i < 1$ at the entire chain; (ii) the Mott-like insulating phase, where the density at the center is kept fixed at $n_i = 1$ and a stronger V potential is required to produce $n_i > 1$; (iii) another metallic phase with $n_i > 1$ at the center of the chain; and (iv) a band-insulator phase, with maximum occupation $n_i = 2$ at the core.

As shown in Fig. 10b, the average single-site entanglement is very well reproduced by DFT calculations in harmonically confined chains. Notice that at $\bar{S}$, the signatures of the distinct phases are very subtle; therefore, in Ref. [46], the entanglement derivative was used to clearly identify the phases induced by the harmonic confinement. But numerical derivatives require a very large number of data to be precise; thus,

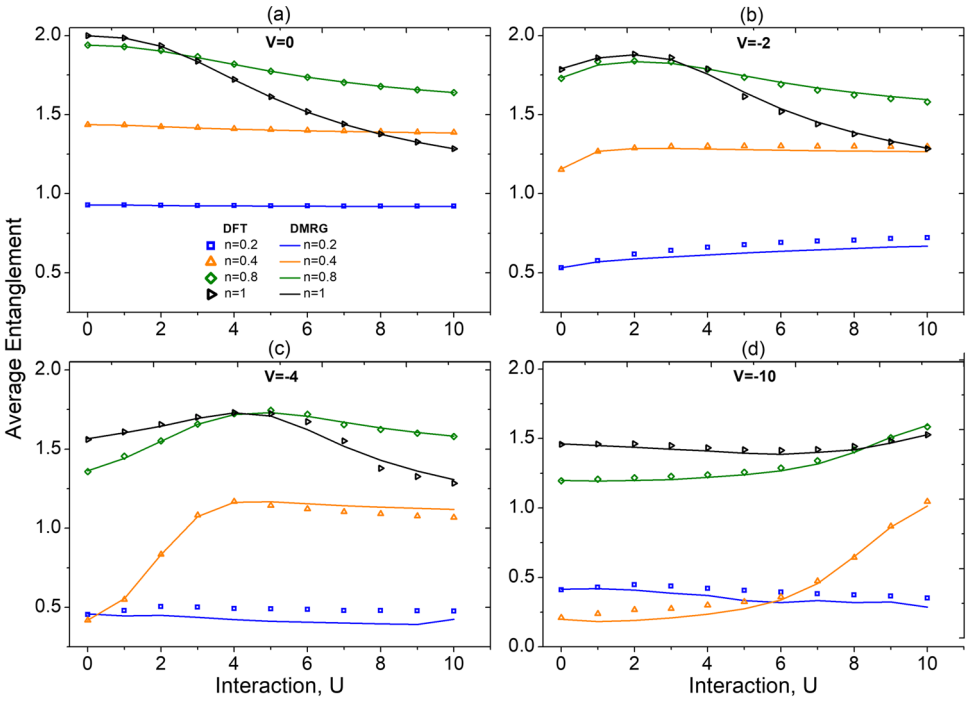

Fig. 8 Average entanglement for a superlattice 2 : 7 with $L = 90$ sites as a function of the on-site interaction, for several densities and distinct periodic potential strengths: **a** $V = 0$, **b** $V = -2$, **c** $V = -4$, and **d** $V = -10$

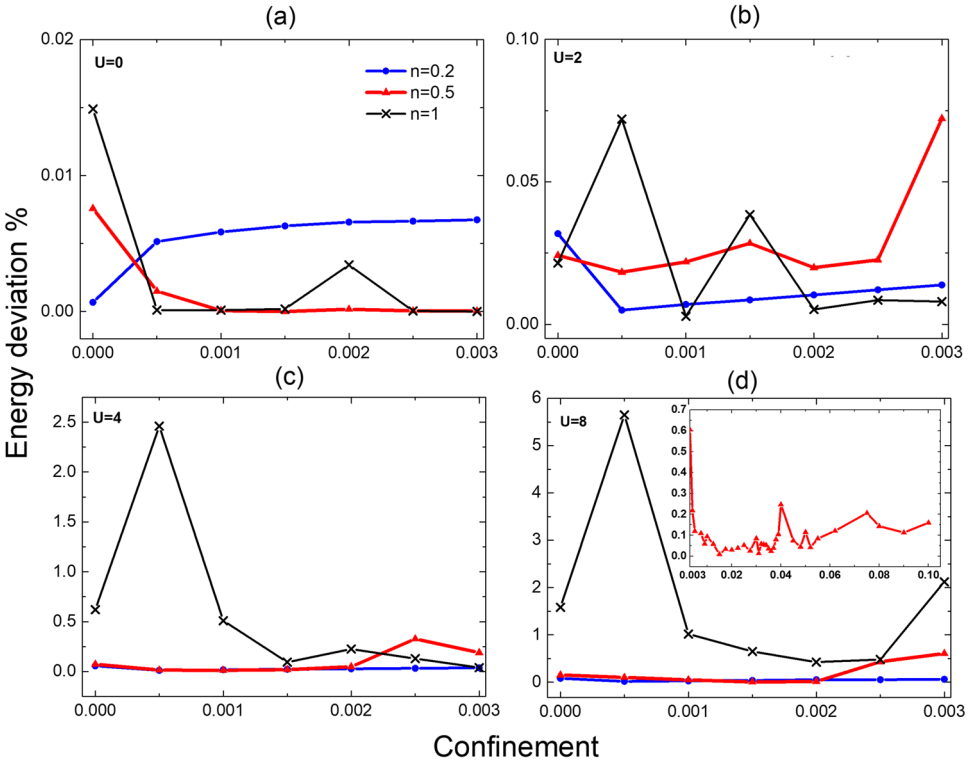

Fig. 9 DMRG-DFT deviation for the ground-state energy as a function of the confinement curvature k for several densities and interactions: **a** $U = 0$, **b** $U = 2$, **c** $U = 4$, and **d** $U = 8$. The inset shows the energy deviation at $n = 0.5$ for larger confinement strengths, as explored in Fig. 10

we here propose an alternative analysis to the transitions, which consists of considering the average single-site entanglement only at the effective chain, $\bar{S}_{eff} \equiv \bar{S}(n_i > 0.001)$, i.e., for the sites that are effectively occupied. Figure 10b reveals that $\bar{S}_{eff}$ signs better the distinct phases: it decreases monotonically with k in the metallic phase (i); has a local minimum at the Mott-like transition (ii); a local maximum at the metallic regime (iii); and a monotonic decreasing for the band-insulator phase (iv).

Finally in Table 1, we present the deviations for a few representative cases of each of the systems, homogeneous, superlattices, and harmonic confinement, for strongly correlated systems with $U = 8$, which represents a challenge to DFT calculations. In general, one finds that the deviations for the density profile are greater than the deviations for the ground-state energy and entanglement for all the systems. We attribute this to error cancellations related to the under and overestimate of DFT for the density profile, while Eq. 9

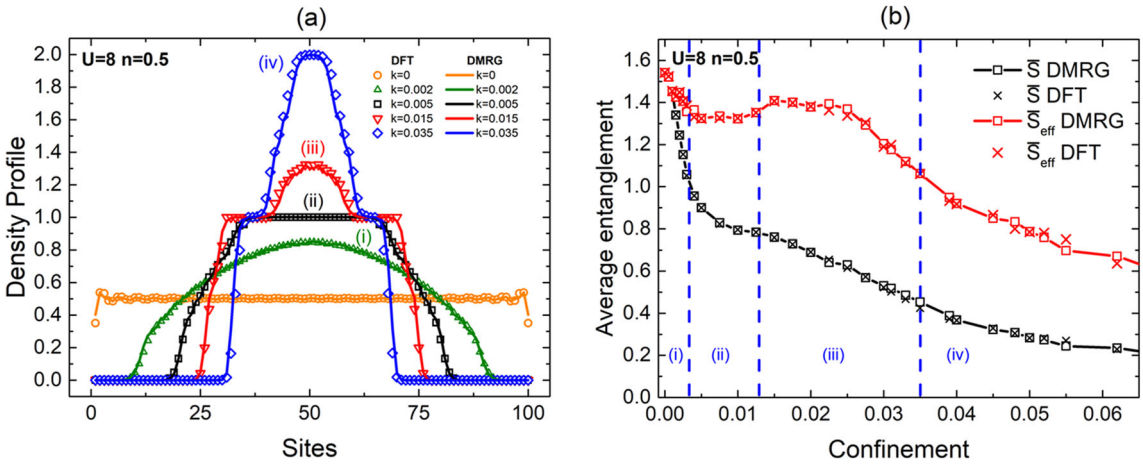

Fig. 10 **a** Density profile for confined lattices, with $L = 100$ sites, for several confinement curvatures k. **b** Entanglement as a function of the confinement curvature k: averaging over the entire chain, $\bar{S}$, and averaging only at the effective chain (central sites with occupation $n_i > 0.001$), $\bar{S}_{eff}$. While in both cases DFT reproduces the DMRG data, one sees that $\bar{S}_{eff}$ is more sensitive to the transitions between the phases: (i) metallic, (ii) Mott-like insulating, (iii) metallic at the center of the chain, and (iv) band insulating at the core

Table 1 Deviations for the ground-state energy (Eq. 7), the average entanglement (Eq. 8), and the density profile (Eq. 9), for homogeneous chains ($U = 8, n = 0.6$) of distinct sizes L, superlattices ($U = 8$, $n = 0.4$, $V = -2$, $L = 36$) with different structures SL, and harmonic confinement ($U = 8$, $n = 0.5$, $L = 100$) for distinct curvatures k

	GS energy $D\%(e_0)$	Density profile $\bar{D}\%(n)$	Entanglement $D\%(\bar{S})$
Homogeneous			
$L = 10$	2.30	3.09	0.43
$L = 50$	0.44	0.88	0.14
$L = 100$	0.21	0.28	0.11
Superlattices			
SL 2 : 7	1.14	12.05	2.56
SL 3 : 6	1.85	9.60	1.35
SL 4 : 5	1.51	17.19	2.92
Harmonic Confinement			
Metal (i), $k = 0.002$	0.01	2.77	0.16
Mott-like insulating (ii), $k = 0.005$	0.12	3.20	0.02
Metal (iii), $k = 0.015$	0.01	3.15	0.20
band insulator (iv), $k = 0.035$	0.04	13.20	6.62

will always sum up, thus producing a higher average deviation; Eqs. 7 and 8 will have smaller and greater contributions, thus on average producing a small deviation. While for the homogeneous systems, there is a clear hierarchy between the deviations, $D\%(\bar{S}) < D\%(e_0) < \bar{D}\%(n)$, and all the deviations decrease with L; for superlattices and harmonic confinement, the relation among deviations is less trivial and strongly dependent on the SL structure and the confinement strength considered. For the superlattices, in general, DFT calculations become less precise by increasing the number of impurities in the unit cell (3 : 6 and 4 : 5). For the confined chains, DFT performs better for the metallic phases (i) ($k = 0.002$) and (iii) ($k = 0.015$). The highest deviations appear for the band-insulator phase (iv) ($k = 0.035$). At this (iv) phase, the density profile shows essentially only three values, $n_i = 0$ at the chain borders, $n_i = 1$ at the wings of the potential, and $n_i = 2$ at the core (see Fig. 10a), thus any imprecision on the DFT calculations has a bigger impact than in a metallic phase whose density profile is more homogeneously distributed.

Conclusions

We have performed a comparative analysis between DFT and DMRG calculations, focusing on their efficacy in describing the electronic properties and quantum phase transitions of one-dimensional homogeneous, superlattices, and harmonically confined nanostructures.

For homogeneous finite chains, DFT exhibited significant deviations from the DMRG results for chain sizes $L \lesssim 60$, especially for the ground-state energy near the half-filling case: $\sim 16\%$ for small chains $L = 10$, although it is less than 1% for $L \sim 100$. This arises from additional electronic correlations due to Friedel oscillations, which are not very well described by the local density approximation within DFT. However, far from the half-filling case, around 20% band filling, the DFT exhibited the best performance, presenting a maximum deviation of less than 2% for the ground-state energy for any interaction and chain size. Also, there is a clear hierarchy between the deviations, $D\%(\bar{S}) < D\%(e_0) < \bar{D}\%(n)$.

For superlattice and confined systems, the relation among the deviations is less trivial − strongly dependent on the superlattice structure and the confinement strength −, and the inaccuracy of the DFT calculation is amplified, what is justified by the heterogeneous nature of the spatial distribution of electronic occupancy, representing a further challenge to the LDA approach. For the superlattices, in general, increasing the number of impurities in the unit cell represents less precision of the DFT calculations. For the confined chains, DFT performs better for the metallic phases, while the highest deviations appear for the Mott and band-insulator phases.

Although the DMRG offers an accurate description of the wave function of 1D systems, it faces computational constraints that can hinder its scalability to larger nanostructures, while the DFT approach is practicable in arbitrary large systems. Furthermore, DFT results are generally obtained in shorter computational simulation times, typically on the order of minutes, while accurate convergence of the DMRG calculation can reach hours.

This comparative study highlights the importance of leveraging strategies that combine the capabilities of DFT and DMRG to predict electronic properties within one-dimensional nanostructures. Future research efforts can focus on developing hybrid methodologies that synergistically employ the advantages of these approaches, especially in describing the correlation potential [47, 48], thus offering a

more robust and accurate framework for modeling and understanding nanoscale systems.

Acknowledgements This research was supported by FAPESP (2021/06744-8; 2023/00510-0; 2023/02293-7; 2021/02342-2), CNPq (403890/2021-7; 140854/2021-5; 306301/2022-9), Coordenação de Aperfeiçoamento de Pessoal de Nivel Superior - Brasil (CAPES) - Finance Code 001, and by resources supplied by the Center for Scientific Computing (NCC/GridUNESP) from São Paulo State University.

Author Contributions All the authors have contributed equally to the work.

Funding FAPESP (2021/06744-8; 2023/00510-0; 2023/02293-7; 2021/02342-2), CNPq (403890/2021-7; 140854/2021-5; 306301/2022-9).

Data Availability All the data that support the findings of this study are available upon request to the authors.

Declarations

Conflict of interest The authors declare no competing interests.

References

1. Geerlings P, De Proft F, Langenaeker W (2003) Conceptual density functional theory. Chem Rev 103(5):1793–1874. https://doi.org/10.1021/cr990029p
2. Cohen AJ, Mori-Sánchez P, Yang W (2012) Challenges for density functional theory. Chem Rev 112(1):289–320. https://doi.org/10.1021/cr200107z
3. Schollwöck U (2011) The density-matrix renormalization group in the age of matrix product states. Ann Phys 326(1):96–192. https://doi.org/10.1016/j.aop.2010.09.012
4. Kohn W, Sham LJ (1965) Self-consistent equations including exchange and correlation effects. Phys Rev 140:1133–1138. https://doi.org/10.1103/PhysRev.140.A1133
5. Burke K (2012) Perspective on density functional theory. J Chem Phys 136(15):150901. https://doi.org/10.1063/1.4704546. https://pubs.aip.org/aip/jcp/article-pdf/doi/10.1063/1.4704546/14117227/150901_1_online.pdf
6. Mirjani F, Thijssen JM (2011) Density functional theory based many-body analysis of electron transport through molecules. Phys Rev B 83:035415. https://doi.org/10.1103/PhysRevB.83.035415
7. Abedinpour SH, Bakhtiari MR, Xianlong G, Polini M, Rizzi M, Tosi MP (2007) Phase behaviors of strongly correlated fermi gases in one-dimensional confinements. Laser Phys 17(2):162–168. https://doi.org/10.1134/S1054660X0702020X
8. Hu J-H, Wang J-J, Xianlong G, Okumura M, Igarashi R, Yamada S, Machida M (2010) Ground-state properties of the one-dimensional attractive Hubbard model with confinement: a comparative study. Phys Rev B 82:014202. https://doi.org/10.1103/PhysRevB.82.014202
9. Saubanère M, Pastor GM (2011) Density-matrix functional study of the Hubbard model on one- and two-dimensional bipartite lattices. Phys Rev B 84:035111. https://doi.org/10.1103/PhysRevB.84.035111
10. Akande A, Sanvito S (2010) Electric field response of strongly correlated one-dimensional metals: a Bethe ansatz density functional theory study. Phys Rev B 82:245114. https://doi.org/10.1103/PhysRevB.82.245114
11. Arovas DP, Berg E, Kivelson SA, Raghu S (2022) The Hubbard model. Annu Rev Condens Matter Phys 13:239–274. https://doi.org/10.1146/annurev-conmatphys-031620-102024
12. Dutta O, Gajda M, Hauke P, Lewenstein M, Lühmann D-S, Malomed BA, Sowiński T, Zakrzewski J (2015) Non-standard Hubbard models in optical lattices: a review. Rep Prog Phys 78(6):066001. https://doi.org/10.1088/0034-4885/78/6/066001
13. França VV, Vieira D, Capelle K (2012) Simple parameterization for the ground-state energy of the infinite Hubbard chain incorporating Mott physics, spin-dependent phenomena and spatial inhomogeneity. J Phys 14(7):073021. https://doi.org/10.1088/1367-2630/14/7/073021
14. Xianlong G, Chen A-H, Tokatly IV, Kurth S (2012) Lattice density functional theory at finite temperature with strongly density-dependent exchange-correlation potentials. Phys Rev B 86:235139. https://doi.org/10.1103/PhysRevB.86.235139
15. Capelle K, Lima NA, Silva MF, Oliveira LN (2003) Density-functional theory for the Hubbard model: numerical results for the Luttinger liquid and the Mott insulator. In: Gidopoulos NI, Wilson S (eds) The Fundamentals of Electron Density, Density Matrix and Density Functional Theory in Atoms, Molecules and the Solid State. Springer, Dordrecht, pp 145–168
16. Campo VL (2015) Density-functional-theory approach to the thermodynamics of the harmonically confined one-dimensional hubbard model. Phys Rev A 92:013614. https://doi.org/10.1103/PhysRevA.92.013614
17. Saubanère M, Lepetit MB, Pastor GM (2016) Interaction-energy functional of the Hubbard model: local formulation and application to low-dimensional lattices. Phys Rev B 94:045102. https://doi.org/10.1103/PhysRevB.94.045102
18. França VV, Hörndlein D, Buchleitner A (2012) Fulde-Ferrell-Larkin-Ovchinnikov critical polarization in one-dimensional fermionic optical lattices. Phys Rev A 86:033622. https://doi.org/10.1103/PhysRevA.86.033622
19. Qin M, Schäfer T, Andergassen S, Corboz P, Gull E (2022) The Hubbard model: a computational perspective. Annu Rev Condens Matter Phys 13:275–302. https://doi.org/10.1146/annurev-conmatphys-090921-033948
20. Giamarchi T (2003) Quantum Physics in One Dimension, vol 121. Clarendon Press, Oxford
21. Mendes-Santos T, Paiva T, Santos RR (2013) Entanglement, magnetism, and metal-insulator transitions in fermionic superlattices. Phys Rev B 87:214407. https://doi.org/10.1103/PhysRevB.87.214407
22. Paiva T, Santos RR (1998) Metal-insulator transition in one-dimensional Hubbard superlattices. Phys Rev B 58:9607–9610. https://doi.org/10.1103/PhysRevB.58.9607
23. Liu T, He JJ, Yoshida T, Xiang Z-L, Nori F (2020) Non-Hermitian topological Mott insulators in one-dimensional fermionic superlattices. Phys Rev B 102:235151. https://doi.org/10.1103/PhysRevB.102.235151
24. Silva-Valencia J, Miranda E, Santos RR (2002) Luttinger liquid superlattices: realization of gapless insulating phases. Phys Rev B 65:115115. https://doi.org/10.1103/PhysRevB.65.115115
25. Silva-Valencia J, Souza AMC (2012) Entanglement of alkaline-earth-metal fermionic atoms confined in optical lattices. Phys Rev A 85:033612. https://doi.org/10.1103/PhysRevA.85.033612
26. Silva-Valencia J, Franco R, Figueira MS (2013) Quantum phase transition of alkaline-earth fermionic atoms confined in an optical superlattice. Phys Lett A 377(8):643–646. https://doi.org/10.1016/j.physleta.2012.12.042
27. Silva-Valencia J, Franco R, Figueira MS (2009) Entanglement and the ground state of fermions trapped in optical lattices. Phys B: Condens Matter 404(19):3332–3334. https://doi.org/10.1016/j.physb.2009.07.088

28. Silva-Valencia J, Franco R, Figueira MS (2008) The asymmetric Hubbard model with a confining potential: the partial filling case. J Magn Magn Mater 320(14):431–433. https://doi.org/10.1016/j.jmmm.2008.02.079
29. Zanardi P (2002) Quantum entanglement in fermionic lattices. Phys Rev A 65:042101. https://doi.org/10.1103/PhysRevA.65.042101
30. Tichy MC, Melo F, Kuś M, Mintert F, Buchleitner A (2013) Entanglement of identical particles and the detection process. Fortschr Phys 61(2–3):225–237. https://doi.org/10.1002/prop.201200079
31. Canella GA, França VV (2021) Mott-Anderson metal-insulator transitions from entanglement. Phys Rev B 104:134201. https://doi.org/10.1103/PhysRevB.104.134201
32. Fishman M, White SR, Stoudenmire EM (2022) The ITensor software library for tensor network calculations. SciPost Phys. Codebases 4. https://doi.org/10.21468/SciPostPhysCodeb.4
33. Eisert J, Cramer M, Plenio MB (2010) Colloquium: area laws for the entanglement entropy. Rev Mod Phys 82:277–306. https://doi.org/10.1103/RevModPhys.82.277
34. Capelle K, Campo VL (2013) Density functionals and model Hamiltonians: pillars of many-particle physics. Phys Rep 528(3):91–159. https://doi.org/10.1016/j.physrep.2013.03.002
35. Lieb EH, Wu FY (1968) Absence of Mott transition in an exact solution of the short-range, one-band model in one dimension. Phys Rev Lett 20:1445–1448. https://doi.org/10.1103/PhysRevLett.20.1445
36. Essler FH, Frahm H, Göhmann F, Klümper A, Korepin VE (2005) The One-dimensional Hubbard Model. Cambridge University Press, New York
37. Bedürftig G, Brendel B, Frahm H, Noack RM (1998) Friedel oscillations in the open Hubbard chain. Phys Rev B 58:10225–10235. https://doi.org/10.1103/PhysRevB.58.10225
38. Söffing SA, Bortz M, Schneider I, Struck A, Fleischhauer M, Eggert S (2009) Wigner crystal versus Friedel oscillations in the one-dimensional Hubbard model. Phys Rev B 79:195114. https://doi.org/10.1103/PhysRevB.79.195114
39. Arisa D, França VV (2020) Linear mapping between magnetic susceptibility and entanglement in conventional and exotic one-dimensional superfluids. Phys Rev B 101:214522. https://doi.org/10.1103/PhysRevB.101.214522
40. Brünner T, Runge E, Buchleitner A, França VV (2013) Entanglement enhancement in spatially inhomogeneous many-body systems. Phys Rev A 87:032311. https://doi.org/10.1103/PhysRevA.87.032311
41. Coe JP, França VV, D'Amico I (2010) Hubbard model as an approximation to the entanglement in nanostructures. Phys Rev A 81:052321. https://doi.org/10.1103/PhysRevA.81.052321
42. Larsson D, Johannesson H (2006) Single-site entanglement of fermions at a quantum phase transition. Phys Rev A 73:042320. https://doi.org/10.1103/PhysRevA.73.042320
43. Anfossi A, Boschi CDE, Montorsi A, Ortolani F (2006) Single-site entanglement at the superconductor-insulator transition in the Hirsch model. Phys Rev B 73:085113. https://doi.org/10.1103/PhysRevB.73.085113
44. Osborne TJ, Nielsen MA (2002) Entanglement in a simple quantum phase transition. Phys Rev A 66:032110. https://doi.org/10.1103/PhysRevA.66.032110
45. Paviglianiti A, Silva A (2023) Multipartite entanglement in the measurement-induced phase transition of the quantum ising chain. Phys Rev B 108:184302. https://doi.org/10.1103/PhysRevB.108.184302
46. França VV, Capelle K (2006) Entanglement of strongly interacting low-dimensional fermions in metallic, superfluid, and antiferromagnetic insulating systems. Phys Rev A 74:042325. https://doi.org/10.1103/PhysRevA.74.042325
47. Baiardi A, Reiher M (2020) The density matrix renormalization group in chemistry and molecular physics: recent developments and new challenges. J Chem Phys 152(4):040903. https://doi.org/10.1063/1.5129672. https://pubs.aip.org/aip/jcp/article-pdf/doi/10.1063/1.5129672/13277206/040903_1_online.pdf
48. Lubasch M, Fuks JI, Appel H, Rubio A, Cirac JI, Bañuls M-C (2016) Systematic construction of density functionals based on matrix product state computations. New J Phys 18(8):083039. https://doi.org/10.1088/1367-2630/18/8/083039